Additive Manufacturing 36 (2020) 101713

Contents lists available at ScienceDirect

Additive Manufacturing

journal homepage: www.elsevier.com/locate/addma

Research Paper

In-depth comparison of polyamide 12 parts manufactured by Multi Jet Fusion and Selective Laser Sintering

Stefano Rosso [a,b,*], Roberto Meneghello [a,b], Lisa Biasetto [a], Luca Grigolato [b,c], Gianmaria Concheri [b,c], Gianpaolo Savio [b,c]

[a] University of Padova, Department of Management and Engineering, Stradella S. Nicola, 3, 36100 Vicenza, Italy
[b] University of Padova, Laboratory of Design Tools and Methods in Industrial Engineering, Viale G. Colombo, 5, 35131 Padova, Italy
[c] University of Padova, Department of Civil, Environmental, and Architectural Engineering, Via Venezia, 1, 35131 Padova, Italy

ARTICLE INFO

Keywords:
Polyamide 12
Selective Laser Sintering
Multi Jet Fusion
Lattice structure
Fatigue

ABSTRACT

Recently, the possibility of producing medium-to-large batches has increased the interest in polymer powder bed fusion technologies such as selective laser sintering (SLS) and multi jet fusion (MJF). Only scant data about the characterization of parts produced by MJF can be found in the literature, and fatigue behavior studies are absent. This study analyzes the material properties of Polyamide 12 (PA12) powders and printed specimens using both SLS and MJF technologies. The morphology, crystalline phases, density, porosity, dimensional accuracy, and roughness are measured and compared; tensile and fatigue tests are performed to assess the effect of the technologies on the mechanical behavior of the produced structures. In addition, lattice structure specimens obtained by different geometric modeling approaches are tested to understand the influence of modeling methods on the fatigue life. The PA12 powders printed by both SLS and MJF mainly show by X-Ray Diffraction γ-phase and a small shoulder of α-phase. The crystallinity decreases after printing the powders both in SLS and MJF technology. The printed parts fabricated using the two technologies present a total porosity of 7.95% for SLS and 6.75% for MJF. The roughness values are similar, Ra ≈ 11 μm along the building direction. During tensile tests, SLS samples appear to be stiffer, with a lower plastic deformation than MJF samples, that are tougher than SLS ones. Fatigue tests demonstrate higher dispersion for MJF specimens and an enhancement of fatigue life for both SLS and MJF printed lattice structures modeled with a novel geometric modeling approach that allows the creation of smoother surfaces at nodal points. Scanning electron microscopy on fracture surfaces shows a brittle failure for the SLS tensile specimens, a more ductile failure for the MJF tensile specimens, a crazing failure mechanism for the SLS fatigue tested samples, and a crack initiation and slow growth and propagation for the MJF fatigue tested samples.

1. Introduction

The additive or layer-by-layer production of components, in contrast to subtractive manufacturing methodologies, allows for freedom in shape and complexity, reduction of waste, product optimization, production of small batches, and shorter lead times [1,2]. Owing to these recognized capabilities, in 2018, the worldwide additive manufacturing (AM) industry grew 33.5% to $9.795 billion at a rate higher than that in 2017 (21.0%) [3]. Among the materials that can be used with AM techniques, polymers are widely used due to the optimal properties and vast potential of their printed parts, and the advances made in polymer material development are significant [4]. In addition, an analysis of the worldwide material sales data indicates that consumption of polymers for powder bed fusion (PBF) systems represents 26.9% of the total, with a growth from $291 million to $402.1 million in 2018 [3]. This increased interest in the polymer PBF is also driven by the rather new technology called multi jet fusion (MJF). According to international standards [5], SLS and MJF are both PBF technologies. The PBF

Abbreviations: AM, Additive Manufacturing; PA12, Polyamide 12; PBF, Powder Bed Fusion; SLS, Selective Laser Sintering; MJF, Multi Jet Fusion; HSS, High Speed Sintering; SIS, Selective Inhibition Sintering; XRD, X-Ray Diffraction; SEM, Scanning Electron Microscopy; TGA-DSC, Thermogravimetric Analysis and Differential Scanning Calorimetry.

* Corresponding author at: University of Padova, Department of Management and Engineering, Stradella S. Nicola, 3, 36100 Vicenza, Italy.
E-mail address: stefano.rosso.3@phd.unipd.it (S. Rosso).

https://doi.org/10.1016/j.addma.2020.101713
Received 26 June 2020; Received in revised form 9 November 2020; Accepted 11 November 2020
Available online 14 November 2020

manufacturing method can be summarized as follows:

1. a CAD model is sectioned (sliced) at different heights to create layers that contain object sections;
2. the AM machine is initialized by preheating the building platform (mandatory for PBF of polymers, not necessary for PBF of metals);
3. the first layer of powders is evenly distributed on the base plate using a coating mechanism;
4. the 2D slice of the part geometry is fused by selectively sintering the powders that lay on the plate;
5. the base plate is lowered to a height equal to the layer thickness;
6. points from 3 to 5 are repeated until the entire part is built.

The main difference between SLS and MJF lies in the manner how powders are bonded in order to create the solid part; in the SLS process, a laser selectively sinters the powder only in the space defined by a 3D model; in the MJF technology, an array of inkjet print heads releases two types of printing ink: a so-called "fusing agent" is applied inside the model boundaries, while a "detailing agent" is applied at the edges of the model to inhibit the sintering of powders not wetted by the fusing agent and create fine details and smooth surfaces; the layer is then exposed to infrared (IR) heating lights to build the part. The higher speed of MJF technology than SLS is because in SLS the laser sinters the powders point by point, while in MJF the layer is processed line by line, in accordance with the arrangement of the print heads and the infrared lamps. SLS was developed by Carl R. Deckard at the University of Texas [6,7]. MJF can be considered a hybrid between Neil Hopkinson's high-speed sintering (HSS) [8,9] and Behrokh Khoshnevis' selective inhibition sintering (SIS) [10,11]. The former is a technique developed by Loughborough University that aims at sintering 2D profiles of powder layers by adding carbon black that absorbs infrared radiations and increases the rate of sintering, and using an infrared lamp to sinter without the need for a laser. The latter was developed by the University of Southern California and is characterized by the deposition of a sintering-inhibitor liquid along the layer profiles/boundaries to prevent the sintering of selected areas; the uninhibited powder is then sintered by a heated nichrome filament, without the need for a laser. Similarly to the HSS, in MJF the "fusing agent" contains carbon black (5.2%) to absorb infrared radiations, suspended in a solution of water (65%), 2-pyrrolidone (18.7%), and triethylene glycol (8.4%); the "detailing agent", instead, mostly contains water (83%), 2-pyrrolidone (3.7%), and triethylene glycol (11.1%) [12].

SLS process is a mature and widely used material forming technology, thanks to several advantages over other polymer additive techniques [13]. This technology does not require support structures for overhangs and thin walls because the part is supported by the surrounding unfused powders; binders are not required, post-processing steps may be avoided, and there is not a risk of toxicity in biomedical applications [14]; moreover, a variety of materials can be processed using this technique [15,16], from polyamides [17,18] to polyetheretherketone (PEEK) [19]. The SLS processing of polyamide 12 (PA12) has been widely studied. Virgin and reused PA12 powders have been characterized to understand the influence on the microstructure and mechanical properties of printed parts [20,21]; the process parameters have been investigated and optimized to obtain the best mechanical properties and surface finish [22–24]; a 3D failure criterion for SLS PA12 parts undergoing tension, compression, and shear loads as single or combined loads was implemented and verified [25]. Fatigue behavior of SLS PA12 printed parts has been studied under dynamic tension/tension excitation [26], tension/compression excitation [18], four-point rotating bending [27], and load increase method [28], and compared to the PA12 parts obtained with more traditional manufacturing techniques, such as injection molding [29,30]. On the contrary, MJF technology is new in the AM scenario, and few scientific works are available in the literature [31–40]. During the development of the High-Speed Sintering process, Majewski et al. [41] studied the effects of the IR lamp power on the degree of sintering and achievable depth of sintering, eventually concluding that there is a maximum obtainable layer thickness (~200 μm), and that a greater degree of sintering occurs at the higher power levels of IR lamps. Later on, Ellis et al. [42] assessed the influence of print density that corresponds to the amount of "Radiation Absorbing Material" (i.e. carbon black) deposited on the surface, on the crystallinity and mechanical properties of PA12; they found out that when the print density increases, the percentage of crystallinity decreases, while the degree of particle melting increases linearly; moreover, when the print density increases, the stiffness and tensile strength increase, while ductility decreases. For the SIS process, Khoshnevis et al. [11] proposed four theories depending on the inhibitor used: a) macroscopic mechanical inhibition, where droplets of the inhibitor penetrate the powder layer in an impact event, distancing them and avoiding adhesion during the sintering phase; b) microscopic mechanical inhibition, where the inhibitor penetrates the powder layer and obstructs adhesion; c) thermal inhibition, where the inhibitor penetrates the powder layer, cools the polymer particles during the heating step of the process via evaporation and prevents sintering; d) chemical inhibition, where the inhibitor penetrates the powder layer and reacts with the powder particles at their surface, thereby producing a chemical species that is resistant to sintering. Asiabanpour et al. [43] optimized the surface quality and dimensional accuracy of SIS printed parts, setting up a Design of Experiment and using the response surface methodology, studying the effects of several process parameters such as layer thickness, inhibitor liquid pressure and feed rate, heater temperature, and obtaining a mathematical model so as a set of optimized process parameters. They also discussed the inhibitor liquid choice [44] and discarded water, isopropyl alcohol, and other liquids because no inhibition phenomena other than impact cutting and cooling were found, while dichlorobenzene and butylbenzene were not considered due to their toxicity and tendency to damage the printer head system; they found a solution of soluble salt, water, and small amount of alcohol to be the best inhibitor liquid.

O'Connor et al. [31] thoroughly investigated the morphology, chemistry, and mechanical performance of parts produced with MJF technology. The specimens were printed in three build orientations and results showed isotropic behavior in terms of tensile strength with a moderately ductile failure mode. The mechanical properties stayed in the range specified by other works dealing with PA 12 parts. Another study [32] concentrated on the properties of MJF PA12 glass-bead filled parts, showing an increase in the surface roughness and tensile modulus as well as a decrease in the maximum tensile strength and elongation compared to MJF PA12-only specimens; these results were influenced by the poor glass sphere-polymer matrix adhesion. Studies on the water tightness of samples produced with MJF were conducted by Morales-Planas et al. [33], who demonstrated that this technology can be used to produce fluid-handling parts due to the lack of open porosity in their structure, in compliance with ISO standards. Mele et al. [34] investigated the capillarity effect in the MJF process, that comes from the interaction between the detailing and fusing agents, and leads to a non-planar surface, especially when close to the border edges; they first performed experimental measurements on benchmark geometries, and then used the collected data to propose a numerical model.

Habib et al. [35] performed nonlinear finite element analyses to study the compressive response and energy-absorbing characteristics of different lattice structures in both bending-dominated and stretching-dominated cases [45]; they used PA12 samples produced using an MJF machine to conduct the analyses and verify the mathematical model; a comparison between lattices produced with MJF and fused deposition modeling technologies was also done, showing that MJF provides better quality parts in a fraction of the time. Fradl et al. [36] simulated the MJF process with the commercial finite element software Abaqus. They created a modeling framework to predict the thermal behavior, part distortions, and residual stresses at the end of the print by coupling the thermal and mechanical problems. The model was validated using a

medical device as a case study. Kim et al. [46] proposed an approach for the process-level simulation of the MJF technology; they used a cyber-physical system where the cyber part pertains to the printer with the printing controller and process modules, and the physical part is the model of multiple layers of build material; the results of the simulations show a reduction of several orders of magnitude in the computational time when compared with an FEM analysis, while having reasonable accuracy.

Focusing on the comparison between SLS and MJF technologies, only a few studies can be found in the literature. Xu et al. [38] investigated the powders and the performance of PA12 parts fabricated with these two technologies. They found out that the MJF powders have a higher crystallinity and wider sintering window compared to SLS powders; on the other hand, SLS parts have a higher degree of crystallinity, in accordance with the instant heating capability of the laser source; also, SLS parts have better mechanical performance. A similar study was conducted by Sillani et al. [39], in which they compared virgin, reused, and artificially aged powders; they highlighted that MJF powder is end-capped, allowing for higher recyclability of the raw material. Mechanical properties of the printed parts differ slightly from [38]; indeed, in [39], MJF parts have higher elongation at break and higher tensile strength (when printed along z direction), but it is recognized that different process parameters and level of reuse of the powders highly affect the properties of the final parts [20–22,31,47]. Cai et al. [40] proposed a comparison of both the powders and the parts obtained by SLS and MJF technologies. The thermal features, phase constitutions, functional groups, and chemical states of both powders are nearly identical; the printed parts have similar porosity but different pore morphology and volume distributions. A clear anisotropy is detected when changing the printing direction from the XY plane to the Z axis, especially on the UTS, that decreases for the SLS parts and increases for the MJF ones; this different behavior was supposed by the authors to be due to the different sintering approach of the two technologies, with MJF resulting in a better sinter quality between the layers.

It also must be noted that no studies about the fatigue behavior of parts printed with HP MJF have been published yet.

In this work, a comparison between SLS and MJF technologies is presented through the analysis of PA12 powders and printed specimens. Material characterization of powder and samples are obtained by scanning electron microscope, x-ray diffraction, thermogravimetric analysis and differential scanning calorimetry, He-pycnometry, dimensional and roughness measurements, and tensile and fatigue tests, which is the main innovative contribution of this study, especially with regards to MJF technology. Lattice structure specimens obtained by different geometric modeling approaches are also tested to understand the influence of both technologies and modeling methods on the fatigue life; the results obtained from the comparison of the modeling methods depend neither on the material of the part nor on the manufacturing technology, so they can be used as general guidelines when designing parts that require an optimal fatigue behavior. Moreover, the results of the comparison between the two technologies can help both researchers and industry users choose between them, depending on the application and the required mechanical properties.

2. Materials and methods

2.1. Sample preparation

Samples were produced with both SLS and MJF technology. An SLS EOS FORMIGA P110 machine and EOS PA2200-performance [48] PA12 powder were used to produce SLS samples; the powder and process parameters are reported in Table 1; the set of process parameters is a standard set for biomedical applications and was used in a previous work [26]; a similar set of parameters used on the same machine and powders was proved to be one of the best for optimal tensile properties [49]. The HP Jet Fusion 4200 machine and HP3D high-reusability PA12 powder [50] were used to produce MJF samples; the HP machine does not allow parameter modification, and so, the balanced print mode preset was used, consisting of one rolling step and two injection passes spending 10.5 s per layer, as reported in Table 1 [31,33]. For each technology, the powders suggested by the machine vendor (Table 2) were used to achieve the best results. The parts were produced by mixing virgin and reused powders in a refresh ratio (virgin: reused) of 1:1 for SLS, reflecting a standard operating procedure adopted by the lab, and 1:4 for MJF according to the manufacturer's datasheet [50].

Table 1
Process parameters for SLS and MJF process.

	SLS	MJF
Laser beam power	20 W	Balanced mode: one rolling step, two injection passes 10.5 s per layer
Laser scan speed	3000 mm/s	
Layer thickness	100 μm	
Laser spot size	~0.4 mm	
Building platform temperature	160 °C	
Virgin: reused powder ratio	1:1	1:4

For each printing technology, specimens with seven different geometries were manufactured depending on the characterization tests, with shape and dimensions as in Fig. 1. All the specimens belong to the same batch, i.e. the same print job. Three types of lattice structure specimens were designed using different unit cells: cells with a squared section and fillet radius (SF, Fig. 1e), cells with a circular section and fillet radius (CYF, Fig. 1f), and a unit cell obtained by the Catmull–Clark surface subdivision algorithm (CC, Fig. 1g) [26,52]. Adopting the Catmull–Clark subdivision [53], it is possible to obtain a smooth mesh from an initial coarse mesh by recursively applying the algorithm; in CC specimens, three iterations of the algorithm were applied. Lattice structures were obtained by repeating the unit cell along the x, y, and z-axes, three, two, and five times, respectively. The cell dimension is 7.5 mm and the fillet radius is 1 mm for the SF and CYF cells; each cell has a resistant area of 6.25 mm^2, corresponding to a 2.50 mm strut size for the SF cell, and 2.821 mm strut diameter for the CYF cell. The CC cell has a continuous shape variation and the size of the minimum strut section ranges between 2.79 mm and 2.88 mm.

2.2. Powders and sample characterization

A Field Emission Gun electron microscope (FEI Quanta 200 Eindhoven, The Netherlands) in low vacuum mode was used to characterize the powders morphology and the samples after static (Fig. 1c) and dynamic (Fig. 1d–g) mechanical testing. X-Ray diffraction analyses (XRD, Bruker D8 Advance, Mannheim, Germany) were performed on both the starting powders and the rectangular plates (Fig. 1a) using Cu-Kα radiation (scan speed 5°/sec, scan step 0.01) in the range $2\theta = 10^{\circ} - 40^{\circ}$. The powders used during SLS and MJF processes and the core parts of printed cylindrical samples (Fig. 1b) were analyzed by Thermogravimetric Analysis and Differential Scanning Calorimetry (TGA-DSC) using a Mettler-Toledo TGA/DSC 3 + on 5 ± 0.5 mg samples in the range 25–300 °C, at a heating rate of 10 °C/min under nitrogen flow. The crystallinity percentage (C%) was calculated as the ratio between the specific heat of fusion of the sample (J/g) and the specific heat of fusion

Table 2
Properties of used PA12 powders.

	PA2200 Performance (SLS)	PA12 3D High Reusability (MJF)
Density [g/cm^3]	0.440 [38]	0.425 [50]
Powder average size [μm]	56 [51]	60 [50]
Melting point [°C]	176 [48]	187 [50]

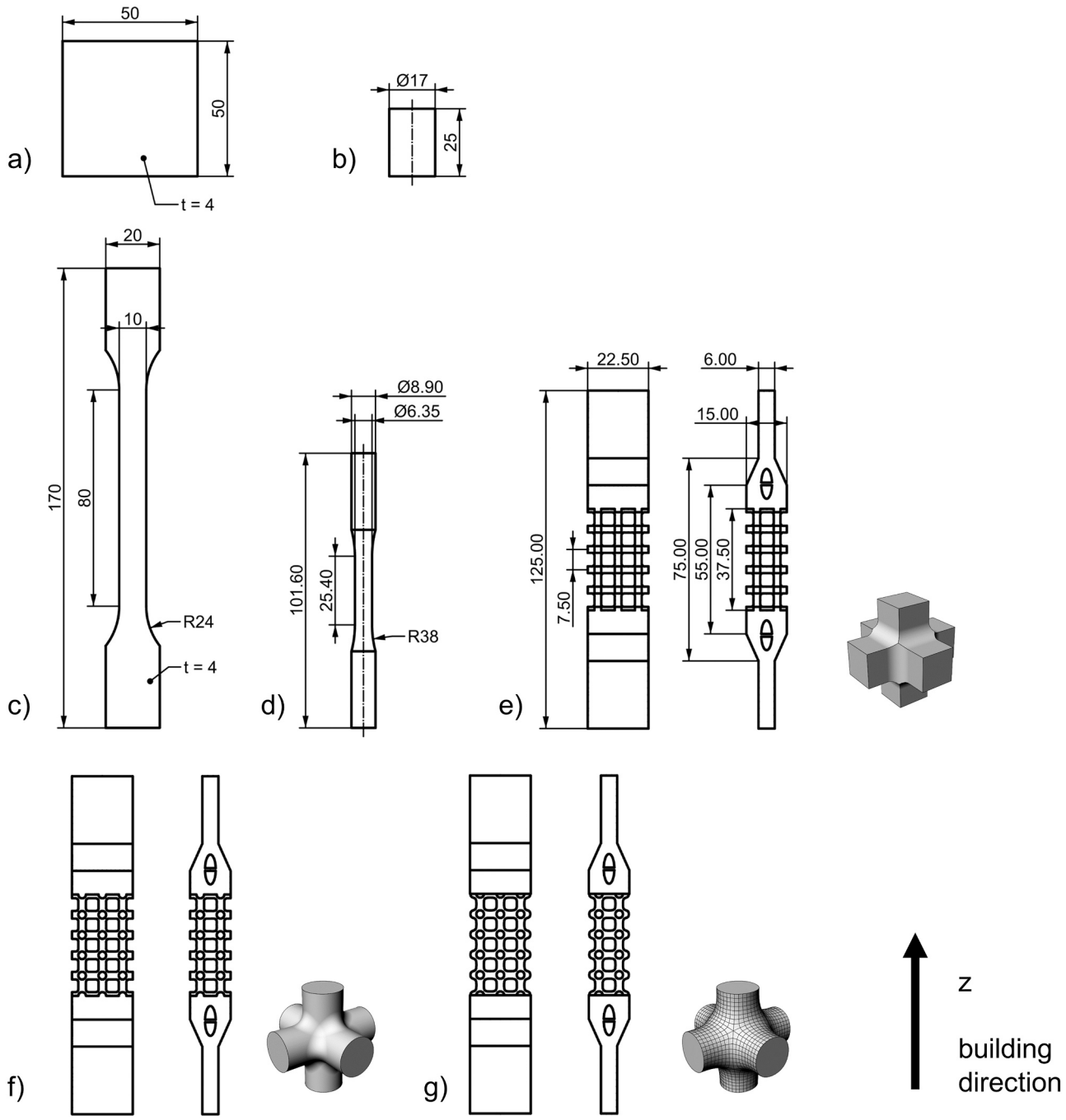

Fig. 1. Specimen dimensions: a) plates for XRD, b) cylinders for He-pycnometry, c) ISO 527 type 1A specimens for static tensile tests, d) ASTM E606 specimens for fatigue tests, e) SF lattice structure for fatigue tests, f) CYF lattice structure for fatigue tests, g) CC lattice structure for fatigue tests. Specimens are in scale.

of 100% crystalline PA12, equal to 209.3 J/g as reported in [54]. The heat of fusion was calculated by the DSC software as integral of the peak. He-pycnometry (Accupyc 1340, Micromeritics) was performed to measure the density of the starting powders (ρ_{th}) and the apparent density (ρ_{app}) of the three cylindrical samples produced by SLS and MJF (Fig. 1b). The bulk density (ρ_{bulk}) of the cylinders was measured as mass over volume ratio, where the mass was measured by a digital balance and the volume by a digital caliper.

The total porosity P_{tot} of the printed parts was calculated as [55]:

$$P_{tot} = 1 - \frac{\rho_{bulk}}{\rho_{th}} \quad (1)$$

The open porosity P_{open} as:

$$P_{open} = 1 - \frac{\rho_{app}}{\rho_{th}} \quad (2)$$

Being the total porosity P_{tot} equal to the sum of open and closed porosity, the closed porosity P_{close} was calculated as:

$$P_{close} = P_{tot} - P_{open} \quad (3)$$

Specimens type 1A that follow the ISO 527 standard [56] (Fig. 1c), specimens adapted from ASTM E606/E606M standard [57] (Fig. 1d), and lattice structures (Fig. 1e–g) were measured with a coordinate measuring machine (OGP SmartScope Flash 200): width and thickness of the ISO 527 specimens central part and diameters of the central part of the ASTM E606 specimens were measured, whereas for the lattice

structures, the size of the struts along the z direction was measured both in the front and in the side view. The error in size was then calculated by the difference between the measured dimensions and the nominal ones. Surface roughness was measured using a Talysurf i-Series on ISO 527 specimens, reporting the Ra parameter (arithmetic mean deviation of the assessed profile) along the growing direction, on the top surface, and on the bottom surface, according to ISO 4287 [58] and ISO 4288 [59] standards (evaluation length = 12.5 mm, sampling length = 2.5 mm).

Mechanical tests were executed on an MTS Acumen 3 Electrodynamic Test System equipped with a 3 kN load cell and an MTS 634.31 F extensometer. Tensile tests were performed according to the ISO 527 standard on five specimens as in Fig. 1c, measuring the mechanical properties of the bulk material at a speed rate of 2 mm/min and with a gauge length of 10 mm. Stress-strain curves and True stress – True strain curves were plotted and Young's modulus, ultimate tensile strength (UTS), strain at break (ε_{max}), and toughness were calculated. The True stress – True strain curves are obtained according to the following equation for the true strain, ϵ, and the true stress σ' [60]:

$$\epsilon = \ln\left(\frac{l}{l_0}\right) \tag{4}$$

$$\sigma' = \sigma(1+\epsilon) \tag{5}$$

where l is the elongation, l_0 is the gauge length, and σ is the engineering

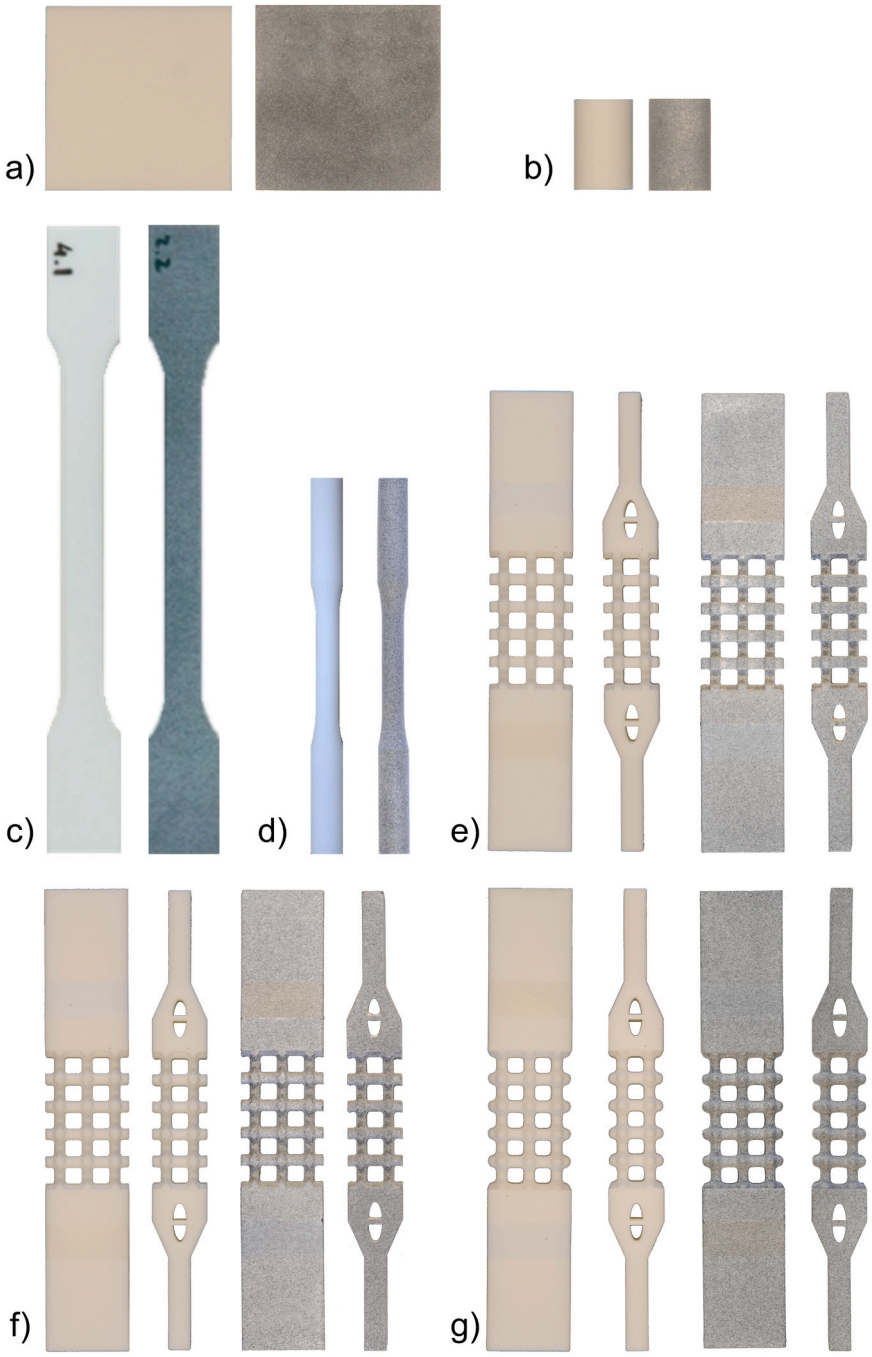

Fig. 2. Printed specimens: a) plates for XRD, b) cylinders for He-pycnometry, c) ISO 527 type 1A specimens for static tensile tests, d) ASTM E606 specimens for fatigue tests, e) SF lattice structure for fatigue tests, f) CYF lattice structure for fatigue tests, g) CC lattice structure for fatigue tests. For each sample, left: SLS, right: MJF. Specimens are in scale.

stress. The material toughness, defined as the area under the true curve until fracture [61], was obtained by:

$$Toughness = \int_0^{\epsilon_f} \sigma' d\epsilon \quad (6)$$

Fatigue tests on SLS and MJF specimens adapted from the ASTM E606/E606M standard (Fig. 1d) and on MJF lattice specimens (Fig. 1e–g) were performed for four load steps (32 MPa, 34 MPa, 36 MPa, 38 MPa) at 3 Hz frequency with zero stress ratio (R = 0, i.e. R = $\sigma_{min}/\sigma_{max}$, where σ is the stress) to avoid buckling phenomena. Data were acquired with a timed trigger at 64 Hz to store signals for the entire cycle and with a peak-and-valley trigger to store the minimum and maximum signals at every cycle. No artificial cooling was applied. Guidelines from the ISO 12107 standard [62] were followed to statistically estimate the stress–number of cycles (S–N) curves, also known as the Wöhler curves. Fatigue tests on SLS SF, CYF, and CC lattice specimens were performed in a previous study [26]. Finally, fracture surfaces of the static tensile tested and fatigue tested cylindrical bulk specimens and lattice structures were analyzed using SEM.

3. Results and discussion

Fig. 2 shows a printed specimen for each type of printing technology (SLS samples on the left, MJF samples on the right) and shape.

3.1. Powders properties and process effect

The SLS and MJF powders used in this study were a mixture of virgin and recycled powders, as recommended by the printers' producers. The reason why producers recommend the use of a mixture of powders lays behind the presence of a mixture of crystalline structures and the consequent positive effect on the mechanical properties of the printed parts [20]. Powders used for SLS can be synthesized in different ways as reported in [20]. SLS polyamide 12 can be obtained by dissolution in ethanol at high pressure and temperature, followed by slow crystallization; alternatively, PA12 powders or granules are heated in steam for a long time (up to 100 h). The main scope of these treatments is to increase the melting temperature of the powders and to improve whiteness and flowability. As an effect, some of the SLS powders show cracks (Fig. 3a). The presence of these cracks is not yet fully understood but it has been supposed to be related to the synthesis process as reported in [21,63]; the evaporation of the remaining ethanol could be a clue. Less is known from the literature on MJF powders, being this an emerging technology. However, the presence of both a melting and a detailing agent on the powder bed is a fundamental prerequisite for the MJF technology. MJF powders regularly come in contact with the solvents of the fusing and detailing agents, but this cracking effect is not as evident as for SLS; this could be explained by the fact that the agents contain 2-pyrrolidone and triethylene glycol, that have boiling points of 251 °C and 288 °C respectively [12], higher than ethanol (78 °C), and the temperature during the printing process does not exceed 185 °C [8,36].

The starting powders and a part of the cylindrical samples were analyzed by TGA-DSC in order to define the melting point and the crystallinity degree. In Fig. 4 both SLS and MJF powders show a single peak corresponding to the melting temperature of 188.6 ± 0.1 °C and 187.7 ± 0.2 °C respectively, as reported in Table 3. These results are in accordance with Cai et. al [40], that used the same PA12 powders, i.e. EOS PA2200 (188.9 °C) and HP PA12 3D High Reusability (188.4 °C), and Schmid et al. [64], that tested 3D-Systems Duraform PA12 powders for SLS machines (186.1 °C), that come from the same PA12 supplier as EOS PA2200, Evonik [65]. In [64] the higher melting temperature of PA12 powders for SLS compared to standard PA12 powders (178 °C) was observed and attributed to the presence of crystalline phases with larger unit cells. Powders for additive manufacturing are subjected to a very special thermal treatment history to enlarge the processability window. The exact thermal cycle of powders is confidential and not revealed by the producers.

The printed samples show a translation of the peak to lower temperature, 183.1 ± 0.5 °C for SLS parts and 182.7 ± 0.4 °C for MJF parts. It is well known from the literature that PA12 may exhibit two crystalline forms. The monoclinic or triclinic α-phase and the pseudohexagonal γ-phase [17]. As reported in [66] films of PA12 showed α-phase with a

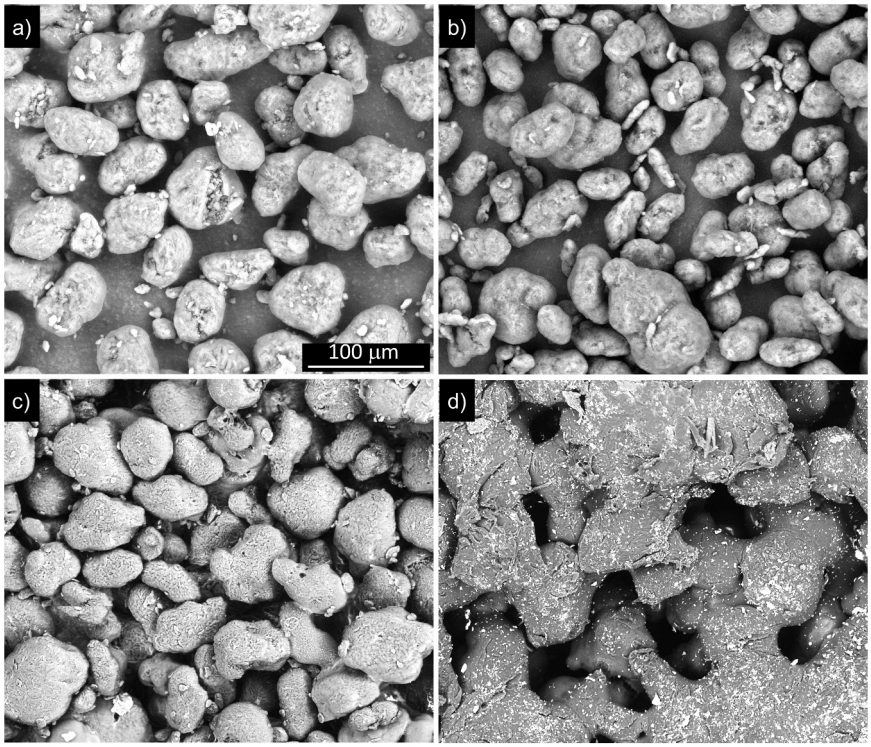

Fig. 3. SEM analyses of the morphology of the powders: a) SLS, b) MJF. Surface morphology of printed parts, c) SLS and d) MJF.

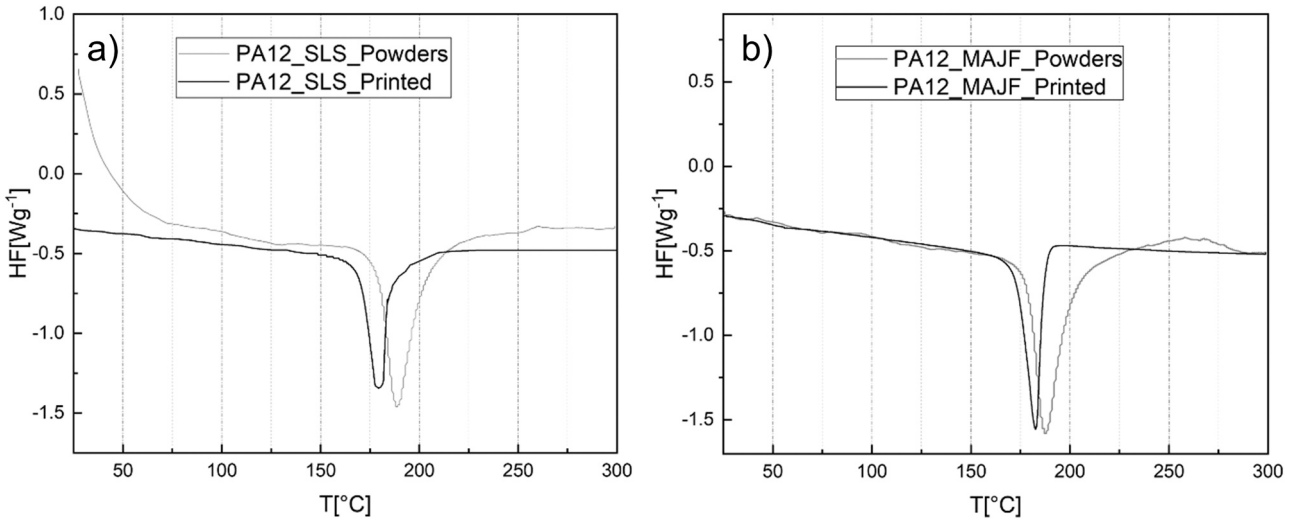

Fig. 4. DSC curves of starting SLS and MJF powders and printed parts: a) SLS, b) MJF.

Table 3
Melting temperature, enthalpy of fusion, and crystallinity of the two sets of samples.

Sample	T_m [°C]	H_m [J/g]	Crystallinity [%]
SLS Powder	188.6 ± 0.1	102.9 ± 1.1	49.1 ± 0.5
SLS Part	183.1 ± 0.5	52.3 ± 0.4	24.5 ± 0.1
MJF Powder	187.7 ± 0.2	101.2 ± 0.9	48.3 ± 0.4
MJF Part	182.7 ± 0.4	65.9 ± 0.3	31.5 ± 0.2

melting temperature of 175 °C, whereas the γ-phase of 182 °C. In this work we used a mixture of starting powders that, as shown later by XRD, are characterized by a mixture of these two phases and values are in accordance with [67].

The calculated crystallinity percentage is reported in Table 3. It can be observed an important decrease of crystallinity both on SLS and MJF printed parts, in accordance with several studies in the literature [21,38,40].

Fig. 5 shows XRD analyses of both starting powders and printed parts. In the starting powders both α-phase and γ-phase are present, whereas after printing mainly γ-phase and a small shoulder of α-phase can be detected. No significant differences emerge between the two technologies in terms of microstructure. This behavior is in accordance with [17,21,29].

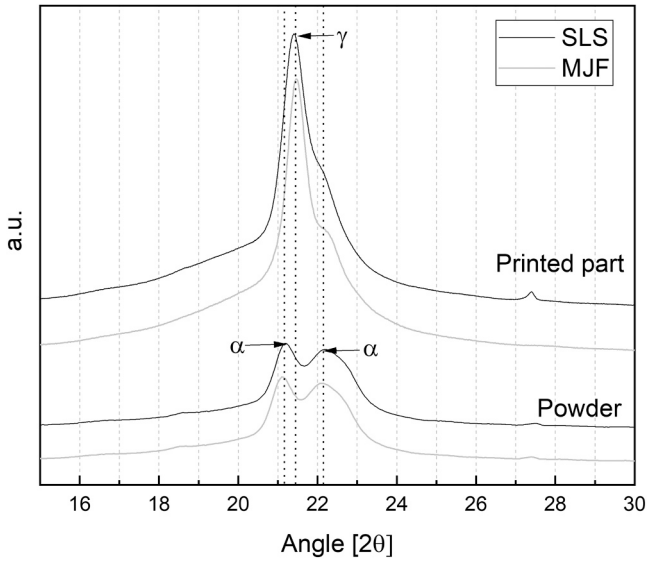

Fig. 5. XRD microstructural characterization of both powders and printed parts (rectangular parallelepiped, as shown in Fig. 1a).

In Table 4, the density of the starting powders (ρ_{th}), the bulk density (ρ_{bulk}), the apparent density (ρ_{app}), the density of the printed parts from the datasheets ($\rho_{datasheet}$), so as the values of the total porosity (P_{tot}), the open porosity (P_{open}), and the closed porosity (P_{close}), calculated by Eqs. (1–3) are reported. The total porosity of SLS printed parts is higher than MJF ones, and this is also reflected in the percentage of closed porosity, 1.61% for SLS printed parts and 1.13% for MJF printed parts. The presence of porosity on PA12 printed parts is well known from the literature, in this study we measured a total porosity higher than average values reported in the literature for SLS and MJF PA12 printed parts [30,31]. A more detailed study on morphological characteristics of porosity is planned in order to assess the pore size distribution, morphology, and their effect on the mechanical performance of the printed parts.

Table 5 shows the mean size error for each type of static and fatigue specimen and technology, obtained by the difference between the measured dimension and the nominal one, as described in Section 2.2. The size error can be positive or negative, depending on the measured size of the sample with respect to the nominal dimension. Lattices produced with SLS present a dimensional error close to 0.1 mm; this does not happen for MJF lattices, where dimensional errors appear to be more dispersed. ISO 527 specimens produced with MJF have the biggest dimensional error, that is, almost one order of magnitude higher than SLS ISO 527 samples. Furthermore, standard deviations are smaller for SLS technology. It has to be highlighted that the samples are embossed and bended [34,38] and these geometrical shape errors induce errors while performing linear measurements. An X-ray computed tomography would allow acquiring the actual printed geometry, and more accurate geometrical information would be available.

Table 4
Density and porosity for SLS and MJF samples.

Property	SLS	MJF
ρ_{th} [g/cm^3]	1.058 ± 0.001	1.056 ± 0.001
ρ_{bulk} [g/cm^3]	0.974 ± 0.011	0.985 ± 0.025
$\rho_{apparent}$ [g/cm^3]	0.991 ± 0.002	0.997 ± 0.011
$\rho_{datasheet}$ [g/cm^3]	0.93	1.01
P_{tot} [%]	7.95 ± 0.09	6.75 ± 0.18
P_{open} [%]	6.35 ± 0.01	5.62 ± 0.06
P_{close} [%]	1.61 ± 0.10	1.13 ± 0.24

Table 5
Size error of samples used for mechanical tests.

	SLS	MJF
	Size error [mm]	Size error [mm]
ISO 527	0.034 ± 0.035	0.319 ± 0.079
ASTM E606	0.052 ± 0.030	-0.053 ± 0.069
SF	0.099 ± 0.031	0.053 ± 0.061
CYF	0.095 ± 0.030	-0.091 ± 0.050
CC	0.089 ± 0.043	-0.084 ± 0.080

Table 6 shows the measured roughness profile (Ra) on the top face, bottom face, and building direction of the ISO 527 specimens, for both technologies. As previously observed for SLS [26], MJF specimens present a rougher surface on the bottom face compared to the building direction. Usually, surface roughness in the building direction is higher than at the top surface [30], but it has been shown that the results are highly dependent on the process parameters, filter wavelength, and measurement techniques [27]. In [31], specimens produced by MJF technology presented greater roughness on the top surface Ra = 10.29 μm) than the bottom surface Ra = 2.54 μm); however, they were glass-bead blasted prior to the experiment. In the present study, the specimens were not post-processed, and partially un-melted powder could stick to the part and modify the surface texture, especially on the bottom face.

Fig. 6 shows the results of the tensile tests on ISO 527 specimens, generating both the engineering (Fig. 6a and d) and true (Fig. 6b and e) stress–strain curves. The tensile behavior of the tested samples is reported in the tables is Fig. 6c and f: the Young's modulus is similar for the two sets of samples, with SLS showing stiffer behavior. MJF samples, on the other hand, show a more ductile behavior that is expressed by a deformation at break of 30% versus the 10% of samples printed by SLS. The UTSs of the two technologies overlap. The MJF samples show a higher toughness.

The results of the tensile tests are supported by the SEM analyses performed on the fracture surface of the ISO 527 specimens (Fig. 7). The SLS specimen, in Fig. 7a and b, shows a brittle fracture surface, brittle fracture paths can be recognized, and hardly any signs of deformation can be distinguished; a similar failure mechanism for SLS parts was noted by Van Hooreweder et al. [18]. The upper part of the fracture surface of the MJF specimen (Fig. 7c and d) shows a ductile fracture surface with signs of plastic deformation, as noted by O'Connor et al. [31], and meets with a smoother lower part where the failure occurs. The ductile fracture of the MJF sample allows for a higher energy absorption before the failure, leading to a higher toughness of the parts, as confirmed by the tables in Fig. 6. Spherical voids are present without distinct PA12 particles in both technologies.

A comparison between the obtained mechanical properties and data available in the literature can be found in Table 7. SLS results are in accordance with other studies, except for the high elongation at break found by Xu et al. [38] and Cai et al. [40] but in both cases the specimens were printed with different orientations (on the XY plane) with respect to the current work (along Z axis), and the results obtained by Van Hooreweder and Kruth [30] where a higher Young's modulus and a lower elongation at break could be explained by the optimization of parameters to increase the stiffness of the printed parts. Among the available data for MJF, the highest stiffness was obtained by Morales-Planas et al. [33]; even though their specimens were tested according to the ASTM D638–14 standard instead of ISO 527, the specimen dimensions, section area, and test procedures are similar. The results of the current study for MJF printed parts present a slightly higher Young's modulus than that obtained in previous studies, and an elongation at break similar to the elongation of the samples printed along the Y axis (YZ plane) obtained by O'Connor et al. [31], and the ones printed along X axis (XY plane) by Cai et al. [40]. Considering studies that compare SLS and MJF technology, MJF samples tougher than SLS ones were also found in Sillani et al. [39], but the set of parameters for SLS was optimized for the best surface finish and not for the maximum mechanical properties. Also the MJF specimens printed along the Z axis (the same as in the current study) by Cai et al. [40] presented a higher UTS and Young's modulus than SLS specimens. Xu et al. [38] obtained a behavior that is in contrast: SLS parts have higher Young's modulus, UTS, and elongation than MJF. This behavior could be due to the different orientation of the printed samples, namely, flat in Xu's research and along the building direction in the present one; indeed, the mechanical properties of MJF printed parts were found to differ depending on the building direction [31,33]. Furthermore, the differences between the results mentioned in the literature are because of the possible differences in the experimental conditions, such as temperature and humidity, level of powder reuse, different set of process parameters for SLS machines, and different firmware that could change the preset configuration for MJF machines.

Table 6
Ra roughness parameter measured on ISO 527 specimens.

	SLS	MJF
	Ra [μm]	Ra [μm]
Top face	10.4 ± 1.6	8.7 ± 0.9
Bottom face	15.0 ± 2.3	13.3 ± 1.0
Building direction	10.8 ± 0.8	11.2 ± 1.2

Fig. 8 shows the S–N curves obtained from fatigue tests. The curves are statistically estimated according to the ISO 12107 standard, for ASTM E606 samples and SF, CYF, and CC lattice specimens, fabricated with both SLS (Fig. 8a) and MJF (Fig. 8b) technologies.

In Table 8 the fitting parameters b_0 and b_1 for the fitting model equation

$$\log_{10}N = b_0 + b_1 \cdot \log_{10}S \quad (7)$$

are reported, together with the standard deviation SD and the correlation parameter R^2.

SLS bulk specimens perform better than MJF ones for stresses higher than 34 MPa. At 32 MPa, the MJF samples fail at a greater number of cycles, approaching the knee of the curve and the fatigue limit. In Fig. 9a and b, the SEM analyses on the fracture surface of the SLS cylindrical samples show a brittle crazing mechanism with large dimple areas, in accordance with Salazar et al. studies [68,69]. The SEM analyses on the MJF specimens fracture surface in Fig. 9c show a different failure mechanism, already described in the literature [70]: the fracture initiates on the contour of the sample, then the crack propagates on the smooth region of the surface, and the final fracture happens on the rough central part of the surface. Porosities are detected in both the technologies, but to a greater extent in the SLS one, in accordance with He-pycnometry measurements in Table 4. Nevertheless, the porosity of a single section does not necessarily reflect the porosity of the entire geometry, especially when considering the section where the failure occurs, where the worst scenario is expected, i.e. higher porosity and defects. Furthermore, the pores do not necessarily affect the fatigue life of thermoplastic materials negatively. When loaded, the porous material deforms and micro-void coalescence occurs; at this point, three possible mechanisms can arise [29]:

1. Local melt zone formation, that stabilizes the crack growth;
2. If the temperature stays under the glass transition temperature, relative sliding between chain molecules occurs, allowing more elasticity;
3. the increasing of the temperature leads to a change in crystalline phases from the γ-form to the α-form; this can cause the molecular chains to shift in a preferential orientation, resulting in an improved fatigue resistance.

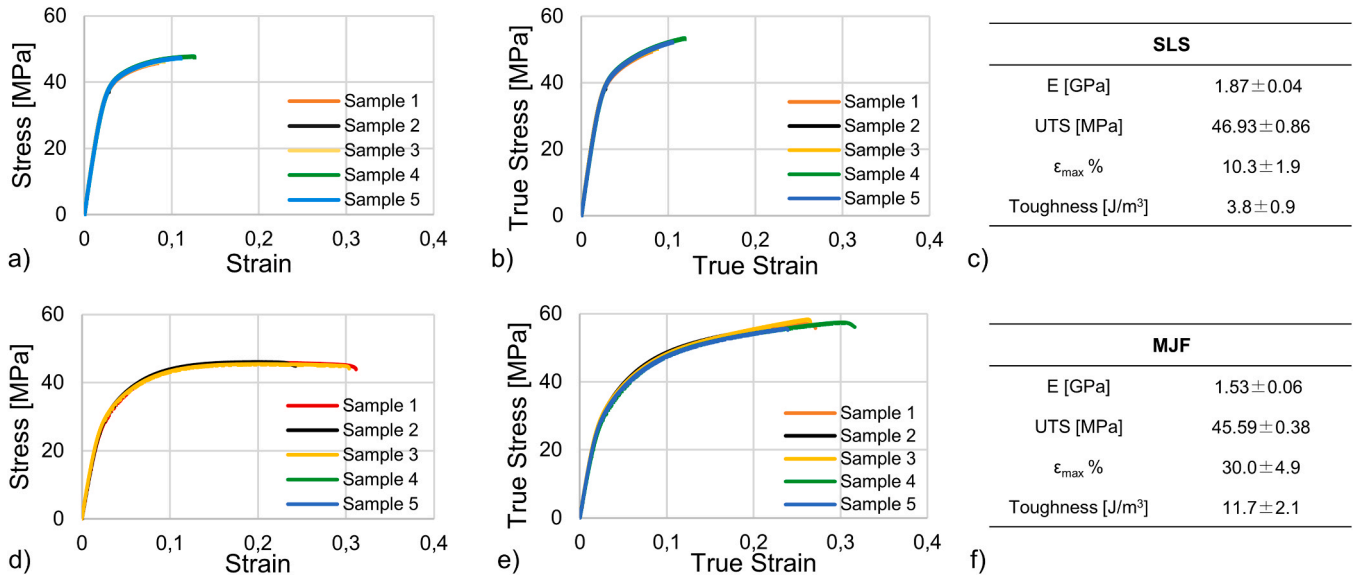

SLS	
E [GPa]	1.87±0.04
UTS [MPa]	46.93±0.86
ε_{max} %	10.3±1.9
Toughness [J/m^3]	3.8±0.9

MJF	
E [GPa]	1.53±0.06
UTS [MPa]	45.59±0.38
ε_{max} %	30.0±4.9
Toughness [J/m^3]	11.7±2.1

Fig. 6. Tensile test curves for ISO 527 specimens. a) SLS Stress–Strain, b) SLS True stress–True strain, c) SLS specimens mechanical properties, d) MJF Stress–Strain, e) MJF True stress–True strain, f) MJF specimens mechanical properties.

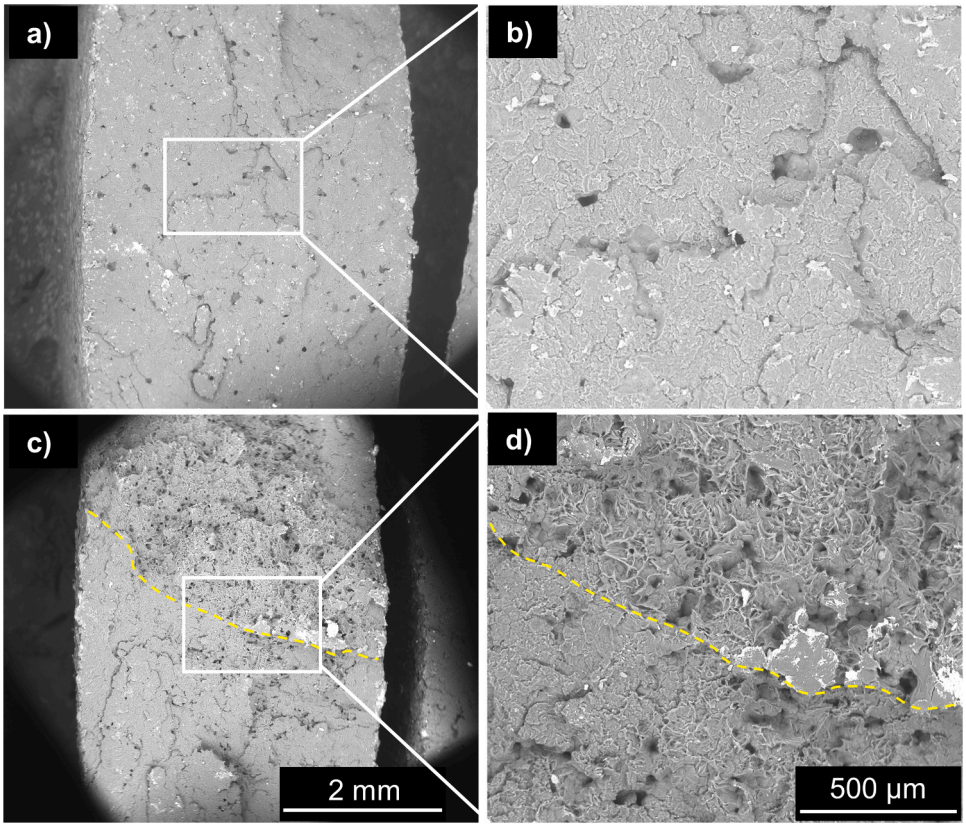

Fig. 7. SEM analyses on fracture surface from static tests on ISO 527 specimens: a) and b) SLS, c) and d) MJF.

To have a wider vision on the phenomenon, further studies are needed where the temperature of the samples in the fracture zone is monitored during the fatigue tests.

Analyzing lattice structures, at high stresses CYF and CC have a behavior similar to the two technologies, but since the slope of MJF is higher, the SLS samples have a longer life at low stresses; the same slope is found in SF samples, but the ones manufactured by MJF have a life behavior better than even CYF, as opposed to SLS where the CYF type behaves better than SF. In general, CC structures show the best behavior between the lattice samples. This is owing to the Catmull–Clark subdivision approach that results in smoother surfaces with respect to standard filleting operations inside the CAD software; as can be seen in Fig. 10, surface curvature for the CC specimens is G2 (curvature continuity), except at extraordinary vertices (i.e. vertices in a quadrilateral mesh in which the number of incident edges differs from 4 [71]), whereas the surfaces of fillets realized with software command are G1

Table 7
Comparison of the tensile properties of PA12 parts, fabricated by powder bed fusion processes.

Technology	E [GPa]	UTS [MPa]	ε_{max} %	Printing direction	Ref.
SLS	1.76 ± 0.02	43.6 ± 0.5	31.6 ± 2.9	XY plane	[38]
	1.68 ± 0.04	47.6 ± 1.4	6.6 ± 0.5	X axis	[39]
	1.61 ± 0.06	40.6 ± 3.2	3.7 ± 0.5	Z axis	
	1.72 ± 0.01	45.1 ± 0.5	10.0 ± 0.1	XY plane	[68]
	1.64 ± 0.01	46.4 ± 0.1	16.9 ± 0.1	X axis	[49]
	2.16 ± 0.05	49.0 ± 1.7	4.0 ± 0.3	Z axis	[30]
	1.39 ± 0.03	44.0 ± 0.1	27.6 ± 2.6	X axis	
	1.61 ± 0.10	43.9 ± 0.7	26.6 ± 2.9	Y axis	[40]
	1.22 ± 0.03	39.6 ± 0.2	14.7 ± 1.1	Z axis	
	1.87 ± 0.04	46.9 ± 0.9	10.3 ± 1.9	Z axis	(Current study)
MJF	1.42 ± 0.04	40.1 ± 1.5	17.5 ± 3.9	XY plane	[38]
	1.13 ± 0.07	45.8 ± 3.5	11.2 ± 1.8	X axis	[39]
	1.20 ± 0.08	47.9 ± 0.9	13.2 ± 1.5	Y axis	
	1.34 ± 0.10	53.7 ± 1.1	11.4 ± 1.3	Z axis	
	1.24 ± 0.03	47.0 ± 0.9	19.0 ± 2.8	X axis	[31]
	1.15 ± 0.04	48.0 ± 0.8	27.0 ± 1.2	Y axis	
	1.25 ± 0.04	49.0 ± 0.6	16.0 ± 1.9	Z axis	
	3.94 ± 0.36	49.9 ± 1.9	3.3 ± 0.8	X axis	[33]
	3.97 ± 0.31	49.3 ± 3.4	2.2 ± 0.3	Z axis	
	1.37 ± 0.03	48.7 ± 0.8	27.4 ± 2.2	X axis	
	1.37 ± 0.07	44.5 ± 0.7	15.9 ± 1.1	Y axis	[40]
	1.67 ± 0.07	49.6 ± 1.2	14.8 ± 0.3	Z axis	
	1.53 ± 0.06	45.6 ± 0.4	30.0 ± 4.9	Z axis	(Current study)

XY plane is used as the printing direction whether the specimens were printed flat, and no printing direction axes were specified.

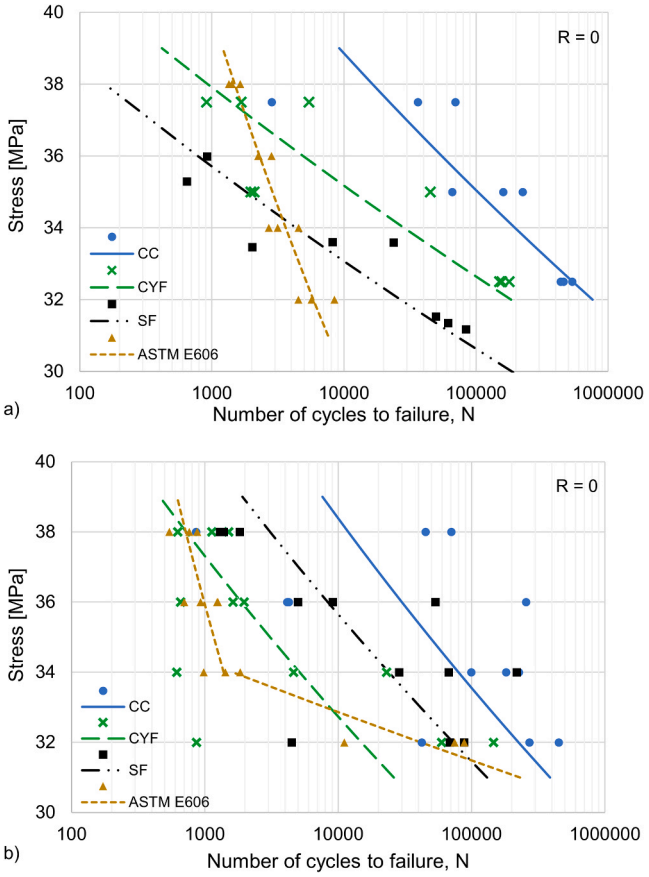

Fig. 8. Wöhler curves obtained from bulk and lattice structures samples: a) SLS, b) MJF.

Table 8
Statistical parameters for S–N curves, according to ISO 12107.

Technology	Specimen type	b_0	b_1	SD	R^2
SLS	ASTM E606	15.79	− 7.99	0.09	0.88
	SF	49.59	− 30.00	0.35	0.89
	CYF	51.58	− 30.77	0.53	0.74
	CC	39.48	− 22.32	0.43	0.69
MJF	ASTM E606	12.13	− 5.88	0.12	0.57
	(ASTM E606 knee)	85.49	− 53.73	0.34	0.85
	SF	32.57	− 18.41	0.60	0.47
	CYF	30.67	− 17.60	0.67	0.39
	CC	31.11	− 17.12	0.74	0.33

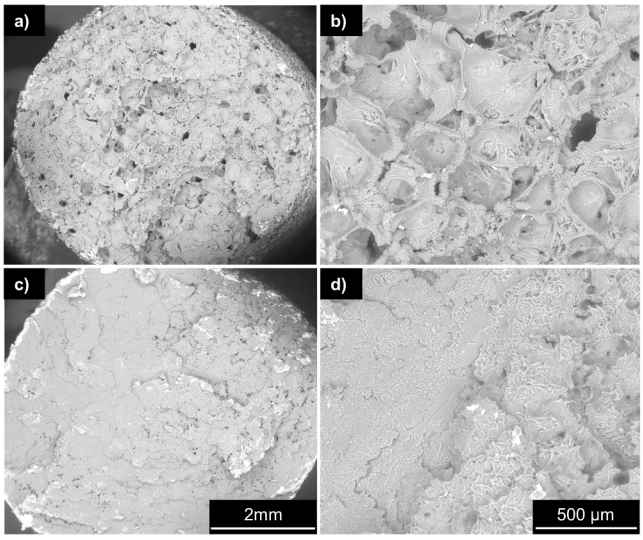

Fig. 9. SEM analyses on fracture surface from fatigue test from ASTM E606 bulk specimen: a) and b) SLS, c) and d) MJF.

(tangency continuity) [26]. This better surface curvature leads to a lower stress concentration and consequently, to a better fatigue life.

Some of the lattice specimens, especially the CC type, behave better than bulk ones, as opposed to the observations of a previous study that used selective laser-melted 316 stainless steel parts [72]. The different behavior could be explained firstly by the difference in the materials used (polymers vs metals) and secondly, by a scale effect due to the different size of the beams of the lattice structures; indeed, bigger beams as in PA12 specimens could help avoid failure driven by internal defects and porosities that reduce the effective area on a cross-section, and surface texture where roughness represents a weakness [28,73]. SEM analyses on the fracture surface of the different types of lattice structures confirm the failure mechanisms observed for the ASTM E606 specimens. The SLS lattices show the brittle crazing mechanism, especially the SF lattices (Fig. 11a) and the CC lattices (Fig. 11c), while the MJF lattices present more planar surfaces where the crack propagated before the failure of the samples. Some dimples are found in the MJF CYF specimen (Fig. 11e).

4. Conclusions

In this work, a comparison between SLS and MJF technologies used to produce PA12 components is presented. Both the powders and the printed parts underwent different experimental tests to characterize the microstructure and morphology; the printed parts also underwent dimensional and roughness measurements as well as mechanical and fatigue tests. In addition, fatigue tests on three types of lattice specimens were performed; the lattices were obtained by the regular repetition of a simple cubic unit cell, but each type of unit cell was geometrically

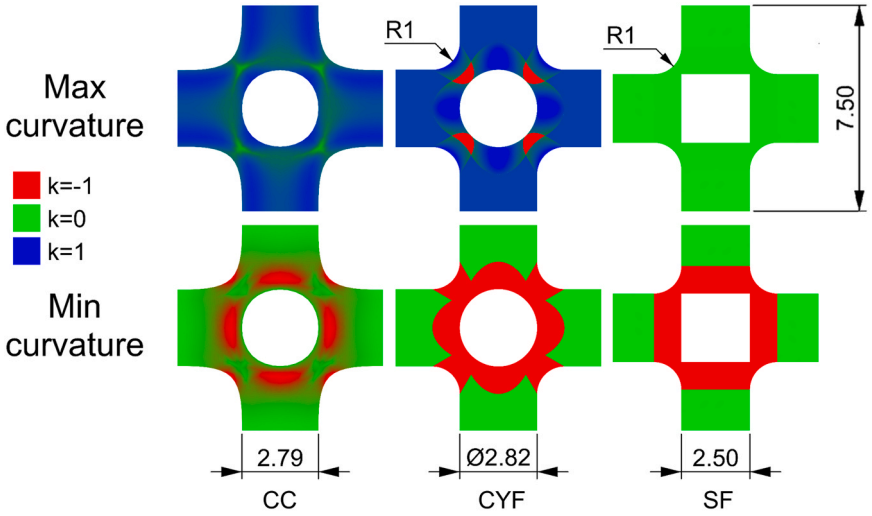

Fig. 10. Surface curvature analysis results performed on the lattice structures unit cells.

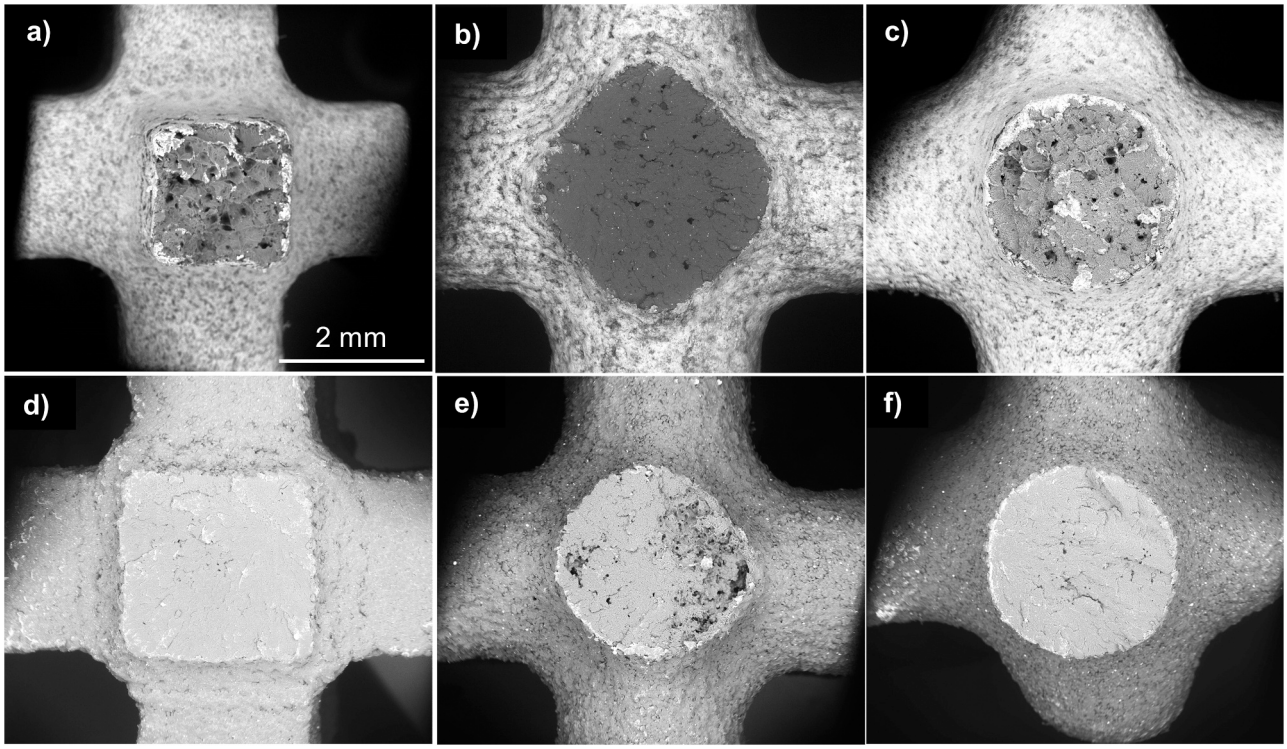

Fig. 11. SEM analyses on fracture surface of fatigue tested lattice structure specimens: a) SF SLS, b) CYF SLS, c) CC SLS, d) SF MJF, e) CYF MJF, and f) CC MJF.

modeled by adopting different approaches, resulting in three different filleting designs at nodal points; these modeling procedures do not depend on the material, and the results are applicable not only for parts with different materials, but also for parts fabricated by different processes. The obtained results can be summarized as follows:

- SEM analyses show MJF powders to be smoother than SLS ones. Some of the SLS powders are cracked, probably due to the solution – precipitation process in ethanol, at elevated temperature, used to produce the powders, or due to the evaporation of the remaining ethanol during the printing process.
- TGA-DSC analyses on SLS and MJF powders showed a single peak corresponding to the melting temperature of 188.6 ± 0.1 °C and 187.7 ± 0.2 °C, respectively. The printed samples show a translation of the peak to lower temperature, 183.1 ± 0.5 °C for SLS parts and 182.7 ± 0.4 °C for MJF parts, so as a broadening of the same peak. The crystallinity of the powders, 49.1 ± 0.5% for SLS and 48.3 ± 0.4% for MJF, decreased during the printing process to 24.5 ± 0.1% for SLS and 31.5 ± 0.3% for MJF.
- XRD on both the powders and final parts showed that in the starting powders both α-phase and γ-phase are present, whereas after printing mainly γ-phase and a small shoulder of α-phase can be detected. The microstructure of the two technologies does not show significant differences.
- He-pycnometry measurements indicated a total porosity of the final parts of 7.95 ± 0.09% for SLS and 6.75 ± 0.18% for MJF.
- Roughness measurements on the sample profile (Ra) showed similar values for the two processes, and they both resulted in a rougher

surface at the bottom face (15.0 ± 2.3 μm for SLS and 13.3 ± 1.0 μm for MJF) compared to the lateral face in the building direction (10.8 ± 0.8 μm for SLS and 11.2 ± 1.2 μm for MJF) and the top face (10.4 ± 1.6 μm for SLS and 8.7 ± 0.9 μm for MJF). This can be attributed to the presence of unmelted powders on the surface of the specimens, that did not undergo post-process operations.

- Static tensile tests showed that SLS specimens have a higher Young's modulus than MJF ones (1.87 ± 0.04 GPa for SLS and 1.53 ± 0.06 GPa for MJF), but a smaller deformation at break (0.10 ± 0.02 for SLS and 0.30 ± 0.05 MPa for MJF). The UTSs are similar (46.93 ± 0.86 MPa for SLS and 45.59 ± 0.38 MPa for MJF).
- SEM analyses on the fracture surface of ISO 527 specimens showed a brittle fracture mechanism for the SLS specimens, whereas a ductile fracture for the MJF ones. SEM analyses on fatigue tested cylindrical specimens highlighted a brittle crazing mechanism for the SLS samples, whereas in the MJF parts the crack initiated on the contour and slowly grew until the failure. The failure surfaces of the different types of lattice structures confirmed the fatigue behavior observed on the bulk specimens.
- Focusing on the geometric modeling methods, CC structures show the best behavior among the lattice samples due to the Catmull–Clark subdivision approach, which results in smoother surfaces with respect to standard filleting operations in the CAD software and leads to a lower stress concentration and better fatigue life. The Wöhler curves associated with MJF specimens present lower R^2 values than SLS. Compared to the lattice structures, bulk specimens highlighted better behavior at high stress but a worse behavior at low stress.

CRediT authorship contribution statement

Stefano Rosso: Investigation, Formal analysis, Writing - original draft, Writing - review & editing. **Roberto Meneghello:** Writing - review & editing, Supervision. **Lisa Biasetto:** Investigation, Formal analysis, Writing - review & editing. **Luca Grigolato:** Investigation, Formal analysis. **Gianmaria Concheri:** Supervision, Writing - review & editing, Funding acquisition. **Gianpaolo Savio:** Conceptualization, Project administration, Supervision, Writing - review & editing, Funding acquisition.

Declaration of Competing Interest

The authors declare that they have no known competing financial interests or personal relationships that could have appeared to influence the work reported in this paper.

Acknowledgments

This work was partially funded by Fondazione Cassa di Risparmio di Padova e Rovigo (CARIPARO), Italy, and grant 'BIRD 190850' by the Department of Civil, Environmental, and Architectural Engineering, University of Padova, Italy. The authors gratefully acknowledge generous in-kind support from 3Dfast s.r.l and 3DZ Franchising Limited Treviso for fabricating the test specimens. The authors acknowledge Anna De Marzi (University of Padova, Department of Industrial Engineering) for TGA-DSC measurements.

Data availability

The raw/processed data required to reproduce these findings can be partially shared upon request.

References

[1] J. Holmström, J. Partanen, J. Tuomi, M. Walter, Rapid manufacturing in the spare parts supply chain, J. Manuf. Technol. Manag. 21 (2010) 687–697, https://doi.org/10.1108/17410381011063996.
[2] M.K. Thompson, G. Moroni, T. Vaneker, G. Fadel, R.I. Campbell, I. Gibson, A. Bernard, J. Schulz, P. Graf, B. Ahuja, F. Martina, Design for additive manufacturing: trends, opportunities, considerations, and constraints, CIRP Ann. Manuf. Technol. 65 (2016) 737–760, https://doi.org/10.1016/j.cirp.2016.05.004.
[3] T. Wohlers, I. Campbell, O. Diegel, J. Kowen, T. Caffrey, Wohlers Report 2019, (2019).
[4] L.J. Tan, W. Zhu, K. Zhou, Recent progress on polymer materials for additive manufacturing, Adv. Funct. Mater. 30 (2020), 2003062, https://doi.org/10.1002/adfm.202003062.
[5] ISO/ASTM, ISO/ASTM 52900:2015 (ASTM F2792) - Additive manufacturing – general principles – terminology, (2015).
[6] C. Deckard, Selective Laser Sintering, University of Texas,, Austin, 1988.
[7] C. Deckard, Method and apparatus for producing parts by selective sintering, US4863538A, (1989).
[8] N. Hopkinson, P. Erasenthiran, High speed sintering—early research into a new rapid manufacturing process, in: Proceedings of the Solid Freeform Fabrication Symposium, (2004), pp. 312–320.
[9] H.R. Thomas, N. Hopkinson, P. Erasenthiran, High speed sintering—continuing research into a new rapid manufacturing process, in: Proceedings of the 17th SFF Symposium Austin, TX, (2006), pp. 682–691.
[10] B. Khoshnevis, B. Asiabanpour, M. Mojdeh, B. Koraishy, K. Palmer, Z. Deng, SIS-A New SFF Method Based on Powder Sintering, in: Proceedings of the 2002 International Solid Freeform Fabrication Symposium, (2002).
[11] B. Khoshnevis, B. Asiabanpour, M. Mojdeh, K. Palmer, SIS - a new SFF method based on powder sintering, Rapid Prototyp. J. 9 (2003) 30–36, https://doi.org/10.1108/13552540310455638.
[12] B. Scherer, I.L. Kottenstedde, F.M. Matysik, Material characterization of polyamide 12 and related agents used in the multi-jet fusion process: complementary application of high-resolution mass spectrometry and other advanced instrumental techniques, Mon. Fur Chem. 151 (2020) 1203–1215, https://doi.org/10.1007/s00706-020-02646-x.
[13] R.D. Goodridge, C.J. Tuck, R.J.M. Hague, Laser sintering of polyamides and other polymers, Prog. Mater. Sci. 57 (2012) 229–267, https://doi.org/10.1016/j.pmatsci.2011.04.001.
[14] A. Mazzoli, Selective laser sintering in biomedical engineering, Med. Biol. Eng. Comput. 51 (2013) 245–256, https://doi.org/10.1007/s11517-012-1001-x.
[15] J.P. Kruth, X. Wang, T. Laoui, L. Froyen, Lasers and materials in selective laser sintering, Assem. Autom. 23 (2003) 357–371, https://doi.org/10.1108/01445150310698652.
[16] K.H. Tan, C.K. Chua, K.F. Leong, C.M. Cheah, W.S. Gui, W.S. Tan, F.E. Wiria, Selective laser sintering of biocompatible polymers for applications in tissue engineering, Biomed. Mater. Eng. 15 (2005) 113–124.
[17] G.V. Salmoria, J.L. Leite, R.A. Paggi, The microstructural characterization of PA6/PA12 blend specimens fabricated by selective laser sintering, Polym. Test. 28 (2009) 746–751, https://doi.org/10.1016/j.polymertesting.2009.06.010.
[18] B. Van Hooreweder, F. De Coninck, D. Moens, R. Boonen, P. Sas, Microstructural characterization of SLS-PA12 specimens under dynamic tension/compression excitation, Polym. Test. 29 (2010) 319–326, https://doi.org/10.1016/j.polymertesting.2009.12.006.
[19] M. Schmidt, D. Pohle, T. Rechtenwald, Selective laser sintering of PEEK, CIRP Ann. Manuf. Technol. 56 (2007) 205–208, https://doi.org/10.1016/j.cirp.2007.05.097.
[20] H. Zarringhalam, N. Hopkinson, N.F. Kamperman, J.J. de Vlieger, Effects of processing on microstructure and properties of SLS Nylon 12, Mater. Sci. Eng. A 435–436 (2006) 172–180, https://doi.org/10.1016/j.msea.2006.07.084.
[21] S. Dadbakhsh, L. Verbelen, O. Verkinderen, D. Strobbe, P. Van Puyvelde, J.-P. Kruth, Effect of PA12 powder reuse on coalescence behaviour and microstructure of SLS parts, Eur. Polym. J. 92 (2017) 250–262, https://doi.org/10.1016/j.eurpolymj.2017.05.014.
[22] B. Caulfield, P.E. McHugh, S. Lohfeld, Dependence of mechanical properties of polyamide components on build parameters in the SLS process, J. Mater. Process. Technol. 182 (2007) 477–488, https://doi.org/10.1016/j.jmatprotec.2006.09.007.
[23] S. Singh, V.S. Sharma, A. Sachdeva, S.K. Sinha, Optimization and analysis of mechanical properties for selective laser sintered polyamide parts, Mater. Manuf. Process. 28 (2013) 163–172, https://doi.org/10.1080/10426914.2012.677901.
[24] A. Sachdeva, S. Singh, V.S. Sharma, Investigating surface roughness of parts produced by SLS process, Int. J. Adv. Manuf. Technol. 64 (2013) 1505–1516, https://doi.org/10.1007/s00170-012-4118-z.
[25] P. Obst, M. Launhardt, D. Drummer, P.V. Osswald, T.A. Osswald, Failure criterion for PA12 SLS additive manufactured parts, Addit. Manuf. 21 (2018) 619–627, https://doi.org/10.1016/j.addma.2018.04.008.
[26] G. Savio, S. Rosso, A. Curtarello, R. Meneghello, G. Concheri, Implications of modeling approaches on the fatigue behavior of cellular solids, Addit. Manuf. 25 (2019) 50–58, https://doi.org/10.1016/j.addma.2018.10.047.
[27] J. Munguia, K. Dalgarno, Fatigue behaviour of laser-sintered PA12 specimens under four-point rotating bending, Rapid Prototyp. J. 20 (2014) 291–300, https://doi.org/10.1108/RPJ-07-2012-0064.
[28] M. Blattmeier, G. Witt, J. Wortberg, J. Eggert, J. Toepker, Influence of surface characteristics on fatigue behaviour of laser sintered plastics, Rapid Prototyp. J. 18 (2012) 161–171, https://doi.org/10.1108/13552541211212140.
[29] B. Van Hooreweder, D. Moens, R. Boonen, J.P. Kruth, P. Sas, On the difference in material structure and fatigue properties of nylon specimens produced by injection molding and selective laser sintering, Polym. Test. 32 (2013) 972–981, https://doi.org/10.1016/j.polymertesting.2013.04.014.
[30] B. Van Hooreweder, J.P. Kruth, High cycle fatigue properties of selective laser sintered parts in polyamide 12, CIRP Ann. Manuf. Technol. 63 (2014) 241–244, https://doi.org/10.1016/j.cirp.2014.03.060.

[31] H.J. O'Connor, A.N. Dickson, D.P. Dowling, Evaluation of the mechanical performance of polymer parts fabricated using a production scale multi jet fusion printing process, Addit. Manuf. 22 (2018) 381–387, https://doi.org/10.1016/j.addma.2018.05.035.
[32] H.J.O.' Connor, D.P. Dowling, Comparison between the properties of polyamide 12 and glass bead filled polyamide 12 using the multi jet fusion printing process, Addit. Manuf. 31 (2019), 100961, https://doi.org/10.1016/j.addma.2019.100961.
[33] S. Morales-Planas, J. Minguella-Canela, J. Lluma-Fuentes, J.A. Travieso-Rodriguez, A.A. García-Granada, Multi Jet Fusion PA12 manufacturing parameters for watertightness, strength and tolerances, Materials 11 (2018) 1472, https://doi.org/10.3390/ma11081472.
[34] M. Mele, G. Campana, G.L. Monti, Modelling of the capillarity effect in Multi Jet Fusion technology, Addit. Manuf. 30 (2019), 100879, https://doi.org/10.1016/j.addma.2019.100879.
[35] F.N. Habib, P. Iovenitti, S.H. Masood, M. Nikzad, Fabrication of polymeric lattice structures for optimum energy absorption using Multi Jet Fusion technology, Mater. Des. 155 (2018) 86–98, https://doi.org/10.1016/j.matdes.2018.05.059.
[36] D. Fradl, J. Panditaratne, J. Bi, R. Fu, V. Oancea, Finite element simulation of the Multi Jet Fusion (MJF™) process using Abaqus, Sci. Age Exp. (2017) 440–469. ⟨https://pdfs.semanticscholar.org/fb66/17aab5ff74f47709ebfecb694d32f23ceff2.pdf⟩. accessed January 23, 2020.
[37] https://doi.org/10.1109/CPPS.2016.7483916H. Kim, Y. Zhao, L. Zhao, Process-level modeling and simulation for HP's Multi Jet Fusion 3D printing technology, in: Proceedings of the 2016 1st Int. Work. Cyber-Physical Prod. Syst. CPPS 2016, Institute of Electrical and Electronics Engineers Inc., (2016).
[38] Z. Xu, Y. Wang, D. Wu, K.P. Ananth, J. Bai, The process and performance comparison of polyamide 12 manufactured by multi jet fusion and selective laser sintering, J. Manuf. Process. 47 (2019) 419–426, https://doi.org/10.1016/j.jmapro.2019.07.014.
[39] F. Sillani, R.G. Kleijnen, M. Vetterli, M. Schmid, K. Wegener, Selective laser sintering and multi jet fusion: process-induced modification of the raw materials and analyses of parts performance, Addit. Manuf. 27 (2019) 32–41, https://doi.org/10.1016/j.addma.2019.02.004.
[40] C. Cai, W.S. Tey, J. Chen, W. Zhu, X. Liu, T. Liu, L. Zhao, K. Zhou, Comparative study on 3D printing of polyamide 12 by selective laser sintering and multi jet fusion, J. Mater. Process. Technol. 288 (2021), 116882, https://doi.org/10.1016/j.jmatprotec.2020.116882.
[41] C.E. Majewski, D. Oduye, H.R. Thomas, N. Hopkinson, Effect of infra-red power level on the sintering behaviour in the high speed sintering process, Rapid Prototyp. J. 14 (2008) 155–160, https://doi.org/10.1108/13552540810878012.
[42] A. Ellis, C.J. Noble, N. Hopkinson, High speed sintering: assessing the influence of print density on microstructure and mechanical properties of nylon parts, Addit. Manuf. 1 (2014) 48–51, https://doi.org/10.1016/j.addma.2014.07.003.
[43] B. Asiabanpour, K. Palmer, B. Khoshnevis, An experimental study of surface quality and dimensional accuracy for selective inhibition of sintering, Rapid Prototyp. J. 10 (2004) 181–192, https://doi.org/10.1108/13552540410539003.
[44] B. Asiabanpour, B. Khoshnevis, K. Palmer, Advancements in the selective inhibition sintering process development, Virtual Phys. Prototyp. 1 (2006) 43–52, https://doi.org/10.1080/17452750500289910.
[45] V.S. Deshpande, M.F. Ashby, N.A. Fleck, Foam topology: bending versus stretching dominated architectures, Acta Mater. 49 (2001) 1035–1040, https://doi.org/10.1016/S1359-6454(00)00379-7.
[46] H. Kim, Y. Zhao, L. Zhao, Process-level modeling and simulation for HP's Multi Jet Fusion 3D printing technology, in: Proceedings of the 2016 1st Int. Work. Cyber-Physical Prod. Syst. CPPS 2016, (2016), pp. 1–4. ⟨https://doi.org/10.1109/CPPS.2016.7483916⟩.
[47] M. Pavan, T. Craeghs, P. Van Puyvelde, J. Kruth, W. Dewulf, Understanding the link between process parameters, microstructure and mechanical properties of laser sintered PA12 parts through X-ray computed tomography, (2016).
[48] PA 2200 Performance 1.0, EOS GmbH - Electro Opt. Syst., (2018). ⟨https://eos.materialdatacenter.com/eo/⟩ (Accessed November 18, 2019).
[49] A. Pilipović, T. Brajlih, I. Drstvenšek, Influence of processing parameters on tensile properties of SLS Polymer product, Polymers 10 (2018) 1208, https://doi.org/10.3390/polym10111208.
[50] HP 3D High Reusability PA 12 - Datasheet, (2017). ⟨https://cimquest-inc.com/resource-center/HP/Materials/HP-PA12-Datasheet.pdf⟩ (Accessed February 3, 2020).
[51] EOS, PA 2200 Material data sheet, (2008). ⟨http://www.shapeways.com/topics/udesign/materials/white_strong_flexible/pa2200_material_data_sheet_12_08_en_.pdf⟩ (Accessed September 17, 2020).
[52] G. Savio, R. Meneghello, G. Concheri, Geometric modeling of lattice structures for additive manufacturing, Rapid Prototyp. J. 24 (2018) 351–360, https://doi.org/10.1108/RPJ-07-2016-0122.
[53] E. Catmull, J. Clark, Recursively generated B-spline surfaces on arbitrary topological meshes, Comput. Des. 10 (1978) 350–355, https://doi.org/10.1016/0010-4485(78)90110-0.
[54] S. Gogolewski, K. Czerntawska, M. Gastorek, Effect of annealing on thermal properties and crystalline structure of polyamides. Nylon 12 (polylaurolactam), Colloid Polym. Sci. Kolloid Z. Z. Für Polym. 258 (1980) 1130–1136, https://doi.org/10.1007/BF01382456.
[55] L. Biasetto, P. Zanonato, S. Carturan, P. Di Bernardo, P. Colombo, A. Andrighetto, G. Prete, Lanthanum carbide-based porous materials from carburization of lanthanum oxide and lanthanum oxalate mixtures, J. Nucl. Mater. 378 (2008) 180–187, https://doi.org/10.1016/j.jnucmat.2008.06.016.
[56] ISO International Organization for Standardization, ISO 527–1:2012 - Plastics – determination of tensile properties – Part 1: general principles, (2012).
[57] ASTM, ASTM E606/E606M - 2012 – Standard test method for strain-controlled fatigue testing, (2012).
[58] ISO International Organization for Standardization, ISO 4287:1997 - Geometrical Product Specifications (GPS) – surface texture: profile method – terms, definitions and surface texture parameters, (1997).
[59] ISO International Organization for Standardization, ISO 4288:1996 - Geometrical Product Specifications (GPS) – surface texture: profile method – rules and procedures for the assessment of surface texture, (1996).
[60] R.G. Budynas. Shigley's Mechanical Engineering Design, 10th ed.,, McGraw-Hill Education,, New York NY, 2015.
[61] S. Kalpakjian, S. Schmid. Manufacturing Engineering and Technology, 7th ed.,, Pearson,, 2013.
[62] ISO International Organization for Standardization, ISO 12107:2012 – Metallic materials – fatigue testing – statistical planning and analysis of data, (2012).
[63] L. Verbelen, S. Dadbakhsh, M. Van Den Eynde, J.P. Kruth, B. Goderis, P. Van Puyvelde, Characterization of polyamide powders for determination of laser sintering processability, Eur. Polym. J. 75 (2016) 163–174, https://doi.org/10.1016/j.eurpolymj.2015.12.014.
[64] M. Schmid, A. Amado, K. Wegener, Materials perspective of polymers for additive manufacturing with selective laser sintering, J. Mater. Res. 29 (2014) 1824–1832, https://doi.org/10.1557/jmr.2014.138.
[65] M. Schmid, R. Kleijnen, M. Vetterli, K. Wegener, Influence of the origin of polyamide 12 powder on the laser sintering process and laser sintered parts, Appl. Sci. 7 (2017) 462, https://doi.org/10.3390/app7050462.
[66] T. Ishikawa, S. Nagai, N. Kasai, Thermal behavior of α nylon-12, J. Polym. Sci. Polym. Phys. Ed. 18 (1980) 1413–1419, https://doi.org/10.1002/pol.1980.180180619.
[67] P. Chen, H. Wu, W. Zhu, L. Yang, Z. Li, C. Yan, S. Wen, Y. Shi, Investigation into the processability, recyclability and crystalline structure of selective laser sintered Polyamide 6 in comparison with Polyamide 12, Polym. Test. 69 (2018) 366–374, https://doi.org/10.1016/j.polymertesting.2018.05.045.
[68] A. Salazar, A. Rico, J. Rodríguez, J. Segurado Escudero, R. Seltzer, F. Martin De La Escalera Cutillas, Fatigue crack growth of SLS polyamide 12: effect of reinforcement and temperature, Compos. Part B Eng. 59 (2014) 285–292, https://doi.org/10.1016/j.compositesb.2013.12.017.
[69] A. Salazar, A. Rico, J. Rodríguez, J. Segurado Escudero, R. Seltzer, F. Martin De La Escalera Cutillas, Monotonic loading and fatigue response of a bio-based polyamide PA11 and a petrol-based polyamide PA12 manufactured by selective laser sintering, Eur. Polym. J. 59 (2014) 36–45, https://doi.org/10.1016/j.eurpolymj.2014.07.016.
[70] J.A. Sauer, G.C. Richardson, Fatigue of polymers, Int. J. Fract. 16 (1980) 499–532, https://doi.org/10.1007/BF02265215.
[71] D. Zorin, Subdivision zoo, Subdiv. Model. Animat. (2000) 65–104.
[72] S. Rosso, R. Meneghello, G. Concheri, G. Savio, Scale and shape effects on the fatigue behaviour of additively manufactured SS316L structures: a preliminary study, in: C. Rizzi, A.O. Andrisano, F. Leali, F. Gherardini, F. Pini, A. Vergnano (Eds.), Des. Tools Methods Ind. Eng., Springer International Publishing, Cham, 2020, pp. 879–890.
[73] L. Safai, J.S. Cuellar, G. Smit, A.A. Zadpoor, A review of the fatigue behavior of 3D printed polymers, Addit. Manuf. 28 (2019) 87–97, https://doi.org/10.1016/j.addma.2019.03.023.